Muscovite mica as a growth template of PC$_{61}$BM crystallites for organic photovoltaics†

Jon Feenstra,[ab] Maarten van Eerden, [iD][a] Alexander K. Lemmens,[a] Wester de Poel,[a] Paul H. J. Kouwer, [iD][a] Alan E. Rowan[ac] and John J. Schermer*[a]

Controlling the microscopic organization of active components is crucial for the performance of organic photovoltaic (OPV) cells. In this work, (001) muscovite mica was used as a growth template to study the formation of PC$_{61}$BM crystallites in the active layer structure of OPV cells. The structures were spin-coated from a PC$_{61}$BM : P3HT solution and subsequently annealed. The parameter range to produce layers with high surface density of (sub)micrometer sized PC$_{61}$BM crystallites was significantly larger for mica than for other substrates. The enhanced PC$_{61}$BM nucleation is attributed to an epitaxial relation between the mica surface and PC$_{61}$BM, which was found to crystallise in a hexagonal crystal structure. Through a float-off procedure, the active layer was transferred from the mica substrate to a conductive substrate, which formed the basis of the transferred inverted solar cell. A power conversion efficiency of 2.1% was obtained for this transferred device, which with a 22% higher short-circuit current density outperforms its conventional counterpart that was directly produced on the conductive substrate. A set-up for simultaneous laser beam induced current (LBIC) and surface reflection analysis revealed that the increased current density originates from large circular areas with a radius of about 10 μm around the PC$_{61}$BM crystallites.

1 Introduction

Currently, the most widely used method for the formation of the active layer of fullerene : polymer organic solar cells is the bulk-heterojunction (BHJ) approach.[1,2] In this approach, acceptor- and donor-materials are dissolved in a solvent before this solution is spin-coated onto a substrate. A commonly used acceptor-donor material mixture is phenyl-C61-butyric acid methylester (PC$_{61}$BM) and poly(3-hexylthiophene-2,5-diyl) (P3HT), the molecular structures of which are given in the ESI.† Subsequently, samples are often subjected to different kinds of post-treatments.[3,4] Amongst others, thermal annealing is widely used to improve the morphology of PC$_{61}$-BM : P3HT organic solar cells by crystallization and de-mixing of the P3HT polymer and PC$_{61}$BM molecules.[5,6] A schematic representation of the thus-obtained morphology is shown in Fig. 1a. The phase separation obtained by the post-treatment leads to domains rich in either donor or acceptor materials

that preferably should have a length scale in the range of 10–20 nm.[7–9] However, due to the uncontrolled nature of the phase separation process, a continuously interconnected donor–acceptor network is difficult to obtain. Instead, isolated donor- and acceptor-domains, which are not connected to their corresponding electrodes, are easily formed. Charges dissociated at such 'islands' will not contribute to the photocurrent but will lead to the build-up of space charge, diminishing the device performance (see Fig. 1a).

Furthermore, even though phase separation provides shorter distances for the excitons to diffuse, it is still quite probable that excitons recombine before they dissociate at the interface, simply because the phase domain dimensions are (still) too large (see the right-hand side in Fig. 1a). In addition, due to the bulk-heterojunction morphology, free carriers cannot be transported in straight pathways towards the electrodes, but have to travel longer distances through the donor–acceptor network, increasing the chances of recombination. PC$_{61}$BM agglomeration, commonly referred to as 'PC$_{61}$BM overgrowth', is usually not regarded as beneficial for device performance, because PC$_{61}$BM is not photo-active and the domain volumes of PC$_{61}$BM do not contribute to the absorption of light. Therefore, optimization of PC$_{61}$BM concentration and processing yielding reduced agglomeration was demonstrated to result in performance improvements.[7,10] Nano-scale morphology formation in BHJ cells is predominately caused by P3HT crystallisation which can be

a Radboud University, Institute for Molecules and Materials, Heyendaalseweg 135, 6525 AJ Nijmegen, the Netherlands. E-mail: j.schermer@science.ru.nl
b DNV GL, Utrechtseweg 310, 6812 AR Arnhem, the Netherlands
c University of Queensland, Australian Institute for Bioengineering and Nanotechnology, St Lucia, Qld 4072, Australia

† Electronic supplementary information (ESI) available: Molecular structures of PC$_{61}$BM and P3HT, atomic force microscopy analysis, crystal structure analysis of epitaxially crystallized PC$_{61}$BM, and transmission electron microscopy analysis of epitaxially crystallized be. See DOI: 10.1039/c6ce02492k
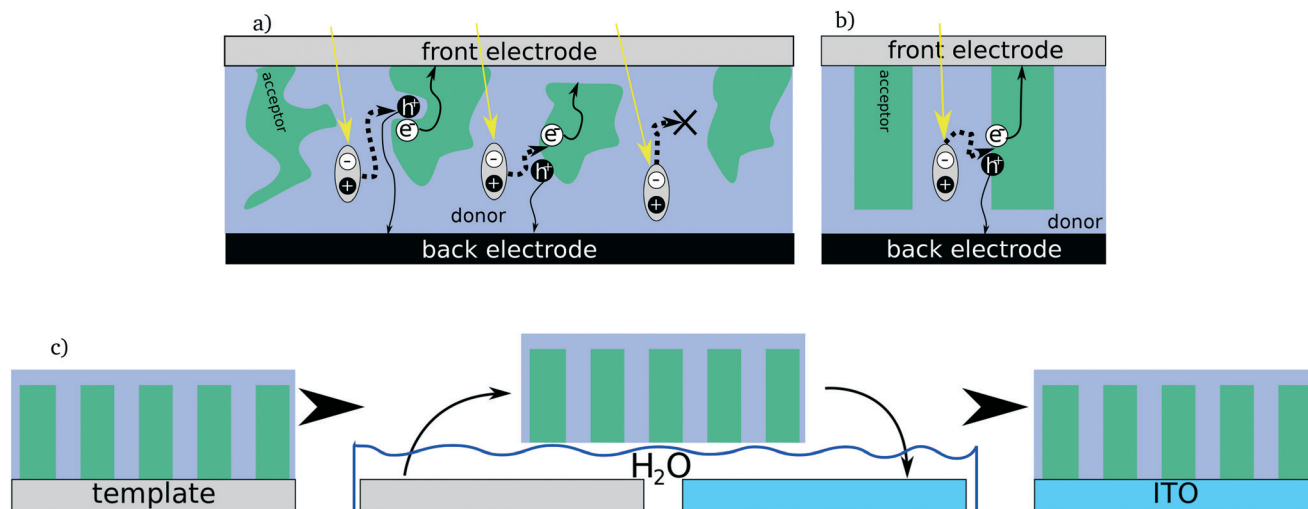
Fig. 1 a) Schematic representation of the bulk heterojunction organic solar cell structure showing exciton formation (upon photon absorption) followed by exciton diffusion and dissociation into free transportable charges and charge transport to the corresponding electrodes (left). The limitations of the BHJ approach, *e.g.* island formation (middle) and limited exciton diffusion (right), are also shown. b) A controlled heterojunction solar cell structure where defined domains of donor and acceptor materials provide an increased probability for exciton dissociation and a clear percolation pathway for free charges. c) The transfer process of an active layer spin-coated and thermally annealed on mica (growth template) floated off by submersion in water and subsequently transferred to, for example, an ITO patterned glass plate. Optionally, additional layers can be applied on the ITO-glass substrate prior to transfer.

controlled by thermal annealing.[6,11–14] Crystalline P3HT regions, already depleted from $PC_{61}BM$, form diffusion barriers and limit excessive growth of $PC_{61}BM$ crystals[11,14] while additionally the power conversion efficiency (PCE) of the solar cells benefits from the crystalline P3HT regions, since local hole mobilities are high compared to amorphous materials.[15–17]

An alternative to the BHJ approach is the application of a controlled heterojunction (CHJ), which is a similar system compared to the BHJ except for the fact that it contains a controlled nano-scale morphology. In the CHJ method, the $PC_{61}BM$ agglomerates are considered desirable. By decreasing their maximum size to twice the exciton diffusion length and increasing their abundance, these agglomerates can improve the device performance, as demonstrated by Yang *et al.*[18] The well-defined domains of donor and acceptor materials present in a CHJ (see Fig. 1b) could overcome the three well-known difficulties of the BHJ (shown in Fig. 1a), namely: exciton diffusion limitations, island formation and indirect percolation pathways for free charges. Ideally, the CHJ would comprise pillar-like acceptor domains separated by (nearly) pure donor domains. If the acceptor pillars are straight and solely connected to one electrode, a clear percolation pathway for dissociated charges towards the electrode is assured. No isolated domains that prevent the loss of photocurrent and the build-up of space charge should be present. An ideal spacing of ~20 nm between the pillars should be able to deliver a sufficient donor–acceptor interfacial area to maximize exciton dissociation. The possible loss of active area in the CHJ approach due to a relatively large coverage of pure, non-absorbing $PC_{61}BM$ domains can potentially be mitigated by employing nano-

structured front electrodes that scatter light diffusively into the cell.[19,20]

Several strategies exist for the formation of small and abundant domains for OPV purposes, for example, molecular stacking of (co-)crystals,[21–23] supramolecular design methods[24] and evaporation-induced deposition.[25] For the small and abundant $PC_{61}BM$ domains to be formed in a configuration such that they can easily come into contact with an external electrode, heterogeneous nucleation of $PC_{61}BM$ on a foreign substrate can be used. Due to interaction with the foreign substrate, the surface free energy of a $PC_{61}BM$ nucleus is lower than for homogeneous nucleation in the bulk and consequently, the activation energy for the formation of a critical $PC_{61}BM$ nucleus is also lower. In the case of an epitaxial relation between $PC_{61}BM$ and the foreign substrate, the interaction between the two is largest and the nucleation rate is highest. For substrate-induced nucleation, $PC_{61}BM$ molecules need to diffuse towards the substrate through the P3HT matrix. Heterogeneous nucleation will always compete with homogeneous (bulk) nucleation, but nucleation at the substrate will dominate when it provides preferred nucleation sites for $PC_{61}BM$. Li *et al.*[26] identified the cleaved surface of muscovite mica normal to the <001> direction to be such a template for structures produced from a $PC_{61}BM:P3HT$ blend. The preferred nucleation property of this template is attributed to the presence of an epitaxial relation between the (001) mica surface and the $PC_{61}BM$ crystals, which Li proposes to crystallize in a distorted cubic lattice.[26] Although the cubic lattice actually does not provide a good match with the mica lattice (see the ESI†), this model was further elaborated by Zheng *et al.*[27] in a study towards the role of the polymer (P3HT) in the $PC_{61}BM:P3HT$ blend and on the shape and

orientation of the $PC_{61}BM$ crystals. In this study, post-deposition annealing was found to be essential and $PC_{61}BM$ diffusion through the blend was recognized as the main determining factor for nucleation and crystal growth.

Because mica is an insulator, the active layer structure after its formation has to be transferred to an electrically active carrier, as shown in Fig. 1c. Li et al.[26] demonstrated the feasibility of this method and reported an enhanced PCE from 0.66%, for a cell directly produced on an ITO coated glass substrate, to 2.23% for a cell of which the active layer was produced on mica, and afterwards transferred to an ITO-glass substrate. This approach shows similarities to the so-called epitaxial lift-off (ELO) process that, since 1995, has been developed in our institute to produce high efficiency thin-film solar cells based on III–V semi-conductor materials.[28] Also, in that case the active layer structure is produced on a dedicated template (usually a GaAs wafer) and afterwards transferred to an electrically active carrier (usually Cu foil that serves as the back contact of the cell). In contrast to the prompt success of organic solar cells as reported by Li and co-workers,[26,27] it took about a decade of research to optimise the lift-off, transfer and subsequent cell processing routines before transferred III–V solar cells were obtained with a performance equal, and later surpassing, that of their regular (i.e. direct on wafer produced) counterparts.[29,30]

For large-scale roll-to-roll applications, the $PC_{61}BM$:P3HT material system is still among the best-performing systems, since it is most compatible with large-area processing.[31] Therefore, inspired by the above described papers of Li et al. and Zheng et al., in the current study $PC_{61}BM$:P3HT mixtures are used for an investigation of in particular the heterogeneous $PC_{61}BM$ crystallisation on muscovite mica in comparison with other substrates as a function of the process conditions applied. The investigated process conditions include the $PC_{61}BM$:P3HT blend composition, annealing temperature and P3HT molecular weight. Although from a PCE perspective 20 nm $PC_{61}BM$ crystallites are most desirable, in this study micrometer sized crystallites are produced by annealing at relatively high temperatures. In contrast to previous investigations, this allows for analysis of the active layers over a, for actual OPV cells, relevant surface area utilizing optical phase contrast microscopy (PCM) and for processed solar cells it allows the assessment of the benefits of $PC_{61}BM$ crystallites to local cell performance using laser beam induced current (LBIC) microscopy. In addition, this approach provides the right crystal size for proper evaluation of the actual $PC_{61}BM$ crystal structure on mica by examination of the orientation of the crystallites with respect to the mica growth template and transmission electron microscopy (TEM) analysis of individual crystallites. It will be shown that rather than the previously proposed distorted cubic lattice, the $PC_{61}BM$ crystallites establish a hexagonal structure. In the case where mica is used to create the active layer structure, solar cells are produced by lift-off and transferring these films to ZnO coated ITO/glass substrates before further cell processing. It is shown that an inverted solar cell with a transferred active layer performs better than its conventional inverted equivalent. This demonstrates the feasibility of the approach to use a dedicated growth template for the production of the active layer structure of an organic solar cell.

2 Experimental

2.1 Sample preparation

In this study, 30×30 mm^2 mica, glass and indium tin-oxide (ITO) patterned glass substrates (for device fabrication) were used. Glass and ITO-glass substrates were cleaned by sequentially sonicating in acetone for 15 minutes, cleaning with a sodium dodecyl sulphate solution, sonicating in this soap solution for 15 minutes, rinsing with ultra-pure water for 15 minutes, sonicating in 2-propanol for 15 minutes and finally applying UV/ozone treatment for 30 minutes. The 30×30 mm^2 mica substrates were cut from larger (001) oriented sheets and simply laterally cleaved under ambient conditions to obtain a freshly cleaved process-ready surface.

$PC_{61}BM$ (Sigma-Aldrich) and P3HT (either in-house synthesized or commercially obtained from Rieke Materials or Sigma-Aldrich) solutions with a total concentration of 20 mg ml^{-1} were prepared by dissolving appropriate amounts in ortho-dichlorobenzene (o-DCB) and stirring overnight at 70 °C. In a nitrogen-purged glovebox, the solutions were spin-coated at 600 rpm for 200 seconds onto the different substrates, and subsequently thermally annealed for 30 minutes on a hotplate at a temperature in the range between 110 °C to 250 °C. The spin-coating process parameters and the annealing time were kept constant for all samples produced in this study. The process parameters that define the production of an active layer sample are the $PC_{61}BM$/P3HT ratio (R), the total concentration of these components in the o-DCB solution (in this study a constant 20 mg ml^{-1} is used) and the annealing temperature (T). For comparison, many samples were produced using $R = 1$ and $T = 140$ °C; these conditions will be referred to as standard process conditions and unless stated otherwise a sample can be considered to be produced under these conditions.

For the transfer of active layers produced on mica to ITO patterned glass or a TEM mesh grid carrier, a water-transfer technique (Fig. 1c) is used. For this purpose, the coated mica substrate was submerged in a nano-pure water bath, in which the active layer simply floated off and was subsequently picked up with another substrate. The transferred active layer was dried at room temperature and subsequently placed on a hot plate at 90 °C for at least 15 minutes to evaporate any remaining water.

2.2 Device processing

It is important to note that solely the spin coating of the active layers and the subsequently applied thermal annealing are carried out in a nitrogen purged glovebox environment. The other equipment for device production and cell analysis is located in ambient atmosphere which is not beneficial to obtaining OPV cells with the highest possible efficiencies.

Therefore we applied a so-called inverted cell configuration (see inset in Fig. 6), which is known to be more stable under ambient conditions.[32] A proof-of-concept study, in which the production of an operational cell from a transferred active layer will be demonstrated. The performance of this cell will be compared with that of a cell directly produced on a patterned ITO-glass substrate. For convenience, we will refer to these cells as transferred inverted cells and conventional inverted cells.

For the device fabrication, the cleaned ITO-patterned glass substrates were coated with the following: a 30 nm zinc oxide (ZnO) electron transport layer, the active layer (either directly spin coated or obtained from transfer), a 30 nm CPP-PEDOT hole transport layer and finally a 100 nm Ag back contact layer to obtain an inverted configuration organic solar cell. The ZnO layer was coated from a solution of zinc acetate dihydrate (0.5 M) and ethanolamine (0.5 M) in anhydrous 2-methoxyethanol, which was stirred for 1 hour prior to spin coating (50 s at 4000 rpm) and annealing (5 min at 150 °C). Zinc acetate dihydrate, ethanolamine and 2-methoxyethanol were obtained from Sigma-Aldrich. After applying the active layer, the samples were further subjected to N_2-plasma for roughly 2 seconds to increase the surface hydrophilicity. The hole transport layer was coated from a solution of 3 : 1 CPP-PEDOT : isopropanol, which was sonicated for 15 minutes and filtered through a 0.45 μm PVDF filter before spin coating (60 s at 6000 rpm) and annealing (10 min at 120 °C). The 100 nm thick Ag back electrode was deposited using a thermal evaporator at a pressure below 10^{-5} bar.

2.3 Analysis

Phase contrast microscopy (PCM) was applied using a Nikon eclipse ME600 microscope equipped with a Nikon digital sight DS-L1 camera. Atomic force microscopy (AFM) images were obtained using a Dimension 3100 system operating with nanoscope (v6.12r1) control units (digital instruments). All images were recorded with the AFM operating in tapping mode in air at room temperature, with a resolution of 512 × 512 pixels and using a scan rate of 1 Hz. Commercial non-contact golden silicon probes (NT-MDT) with a maximum tip curvature radius of 10 nm were used. Gwyddion (v2.31) software was used to convert the raw data into the displayed images. Transmission electron microscopy (TEM) images from samples transferred from mica to a mesh grid were obtained using a JEOL TEM 2100, operated at 200 kV. A GATAN Orius 200D camera was employed to capture the images.

Image analysis was performed on images obtained by PCM and AFM using CellProfiler (v2.1.1) image analysis software. For Fig. 4a, c, and d, each measurement point represents the analysis of 10 images of 175 × 132 μm^2 obtained from a single substrate sample, and for Fig. 2 and 4b, respectively, 3 and 1 image(s) were used for the analysis. For each data point as shown in all images, the average diameter is calculated from all particles in all the images and presented with an error bar representing the

standard deviation. The particle density is determined for the area shown on each image and subsequently averaged over the limited number of images and therefore the error bar was omitted.

To characterize the completed solar cell devices, IV characteristics were obtained using a 2601A Keithley source generator operated with Tracer 3 software by ReRa Solutions. The cells were illuminated using an Abet Sun 2000 solar simulator comprising a 550 W xenon arc lamp light source. The light intensity of the solar simulator was calibrated using a GaAs reference cell. For measurements, the solar cells, with an active area of 0.116 cm^2, were illuminated with an intensity of 1000 W m^{-2} (1 sun). External quantum efficiency measurements were performed using a ReRa Solutions SpeQuest system with an Omni 150 monochromator and a Hg lamp. Calibration was performed using a ThorLabs Si photodiode with known spectral response and a systematic error smaller than 3%. An in-house developed laser beam induced current set-up was used to characterize the local performance of the transferred active layer devices. The set-up includes a 5 mW 633 nm laser which is guided through an optical system before illuminating the cell with a spot of ±1 μm in diameter. During the LBIC measurement, the light reflected from the samples is measured simultaneously.

3 Results

3.1 Morphology and crystal structure

Crystallisation of $PC_{61}BM$ is substrate-dependent, even when no specific crystallographic relation to the substrate is present.[33] Fig. 2 shows the $PC_{61}BM$ crystallisation on three different substrates: ZnO, glass and mica. ZnO was added as a reference as it is the default pre-layer for the active layer in inverted organic solar cells. Image analysis shows that the sample morphologies on ZnO and glass are very similar, indicating that little to no substrate-specific nucleation is present on either substrate. The recipe used to fabricate the ZnO films yields very smooth ($R_{rms} < 2$ nm) and homogeneous ZnO films with a thickness of approximately 30 nm.[34] Both glass (which is amorphous) and ZnO show no crystallographic relation to $PC_{61}BM$, which combined with the smoothness of the substrates explains why no substrate-specific nucleation of $PC_{61}BM$ on these substrates is observed. On the other hand, the sample produced on mica shows significantly smaller crystallites nucleated in a much higher density. If the the size of these crystallites can be further reduced to the 20 nm range by tuning the conditions during processing of the active layer, this morphology could be beneficial for photovoltaic conversion.

Fig. 3 shows a morphology overview of $PC_{61}BM$ crystallites formed at various blend compositions and annealing temperatures when either glass or mica was used as a template. Using PCM clearly identifiable crystallites were formed on both glass and mica when the temperature (T) was at least 140 °C and the ratio $PC_{61}BM/P3HT$ (R) was at least 0.4. However, on glass only at T = 140 °C and R = 1 small round-like
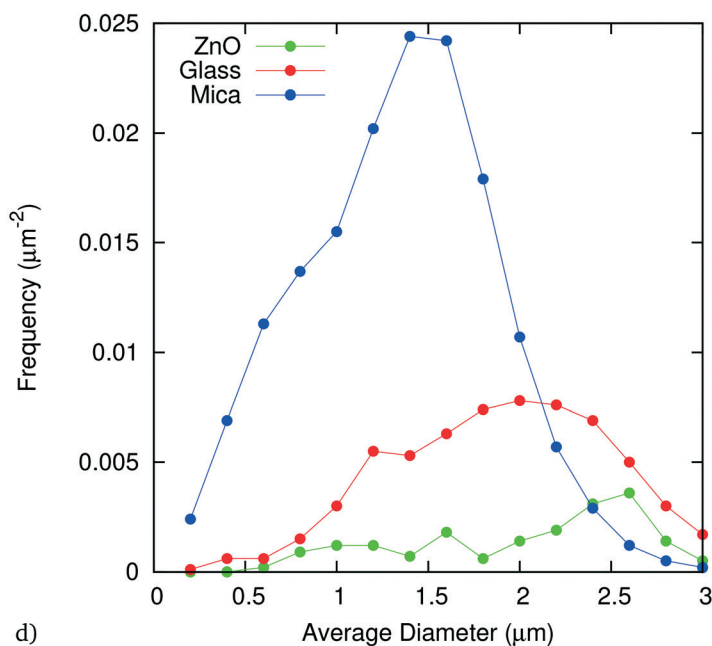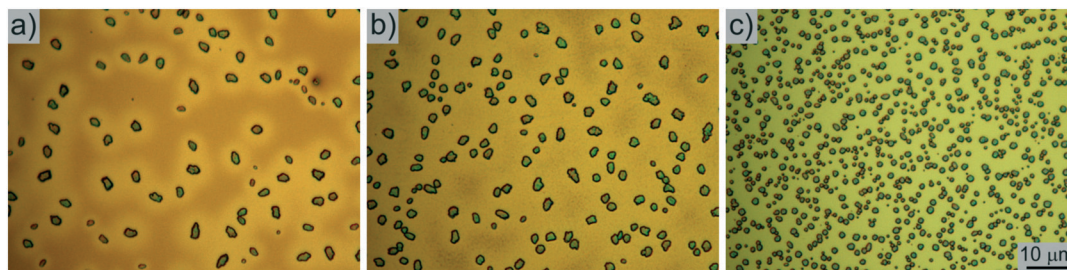
Fig. 2 Optical phase contrast microscopy images (a–c) and $PC_{61}BM$ crystallite particle size distribution (d) for samples produced on ZnO (a, green points), glass (b, red points) and mica (c, blue points) (sample production parameters: $R = 1$, $T = 140$ °C).

crystallites were formed. Both at higher temperatures and increased $PC_{61}BM$ content ($R > 1$), whisker-like crystallites were formed, which can result because of a change in $PC_{61}BM$ diffusion and/or the growth of a different polymorph.[26,35] In contrast, on mica a large range of compositions and temperatures provided round-like crystallites, namely, all samples obtained for $T > 140$ °C and with $R = 1$ as well as $R = 2.5$. At an even higher $PC_{61}BM$ content ($R = 5$), samples on mica are even more densely packed with $PC_{61}BM$ crystallites than for $R = 1$ and $R = 2.5$; however, this is not visible in the optical PCM images of Fig. 3 but is separately shown by AFM analysis (see the ESI†).

The insets in Fig. 3 are enlargements showing the typical crystallite shape, as observed on mica, which becomes more hexagonal with increasing annealing temperature. This is probably related to an increased surface mobility of $PC_{61}BM$ at the growing crystallite at higher temperatures. Rather than random addition of growth units at the location where they arrive, increased surface mobility allows for incorporation at sites that provide a lower surface free energy and hence more pronounced faceted crystallites are formed.

3.2 Temperature dependence

For the formation of $PC_{61}BM$ agglomerates, a temperature threshold of 140 °C was observed for all compositions (see Fig. 3) regardless of the growth template, which is in line with the threshold found by Kim et al.[36] At lower temperatures (110 °C), supersaturation is higher, but $PC_{61}BM$ diffusion is slower so that eventually formed crystallites might be too small to be observed by PCM. Most probably, the limited mobility at low temperatures is related to the high glass transition temperature of $PC_{61}BM$ (ref. 33 and 37) and of PC_{61}-BM:P3HT blends.[38,39] A sharp transition in $PC_{61}BM$ and P3HT diffusion, attributed to changes in the polymer chain mobility, is expected when going up in temperature beyond 130.[40] Indeed, at $T = 140$ °C, there is sufficient diffusion for nucleation to take place and microscopic $PC_{61}BM$ crystallite formation on both glass and mica is observed in this work (Fig. 3 and 4). For even higher annealing temperatures (≥170 °C), whisker-like structures were obtained on glass substrates indicating that diffusion dominates over nucleation.[41] In contrast, on mica, where because of the $PC_{61}BM$–mica interaction heterogeneous nucleation dominates, extensive growth
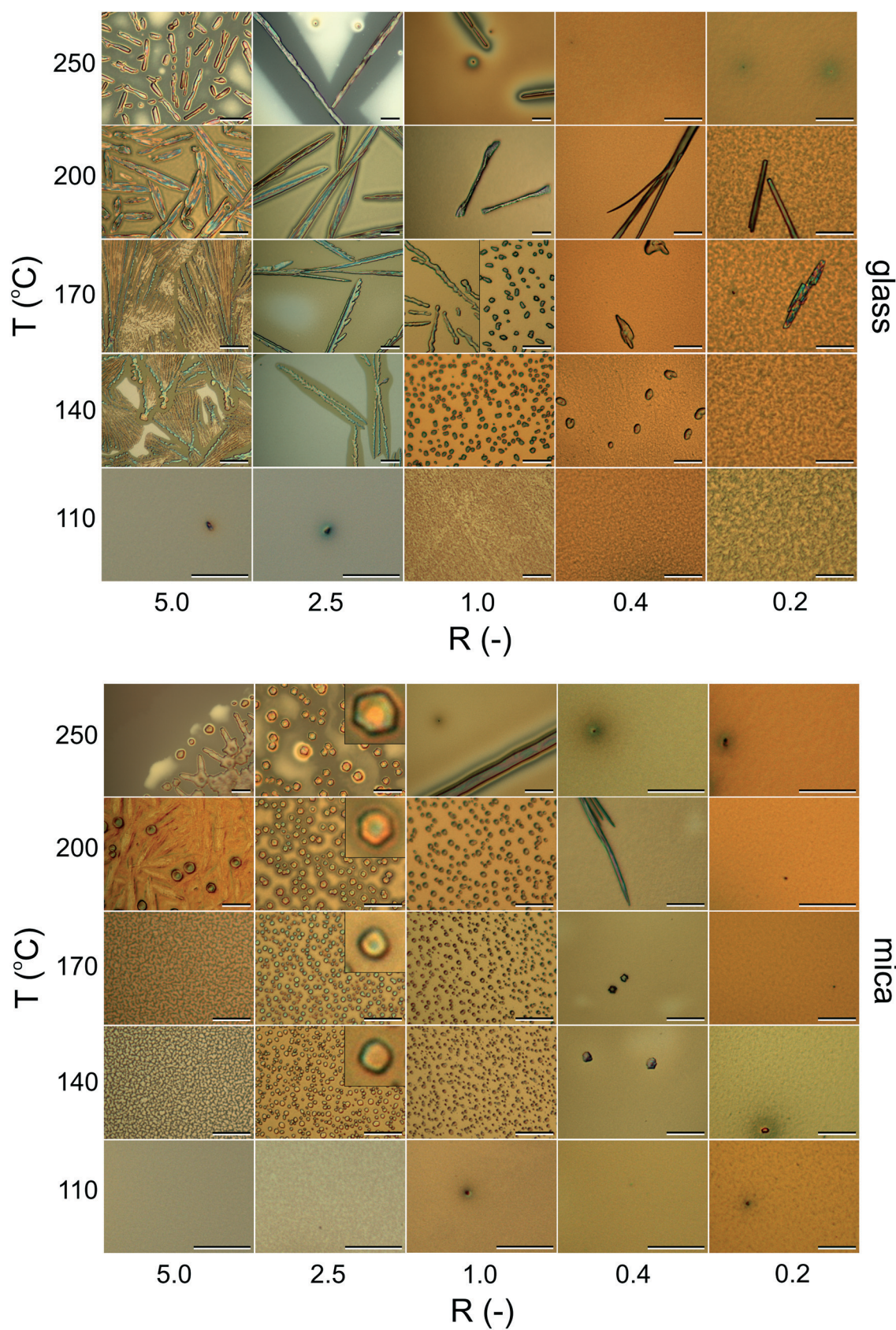
Fig. 3 Phase contrast microscopy overview of the active layer morphology on glass and mica obtained with different $PC_{61}BM$: P3HT ratios at various annealing temperatures. The insets in the mica overview in the 2.5 : 1 row represent a magnification of the typically observed crystallite shape. All markers indicate 10 μm.

is suppressed and small crystallites are formed in large numbers. Whiskers only form on mica at T = 250 °C, where increased diffusion also seems to dominate over the enhanced nucleation of the mica template.

Fig. 4a shows the average diameter and particle density of the $PC_{61}BM$ crystallites formed on mica as a function of annealing temperature for samples produced with R = 2.5 and R = 1 blends. These data were obtained by analyzing 5–10 PCM images per sample, thereby closely representing the morphology across the whole sample. In the ESI† we show that the average particle diameter obtained from PCM images is equal to that obtained from AFM images, justifying our approach to use PCM images to obtain the crystallite characteristics. Generally, the particle density decrease with increasing temperature can be explained by the lower supersaturation of

$PC_{61}BM$ at higher annealing temperatures. This causes the critical nucleus radius and the nucleation barrier to be larger and thus for $PC_{61}BM$ to nucleate less readily. Between T = 140 °C and 170 °C, there seems to be a balance between supersaturation and diffusion, since roughly the same number of crystallites with equal sizes form at both temperatures. This indicates that at T = 140 °C, diffusion is still a limiting factor and at T = 170 °C the lower supersaturation is balanced by the increased diffusion rate. A similar balance between diffusion and supersaturation was found to exist for a blend of $PC_{61}BM$ and a thiophene–quinoxaline polymer,[33] and it is this balance that provides us the relatively small and abundant crystallites at both 140 °C and 170 °C. Samples made at R = 1 and T = 250 °C again resulted in rather large whisker-like structures (see Fig. 3).
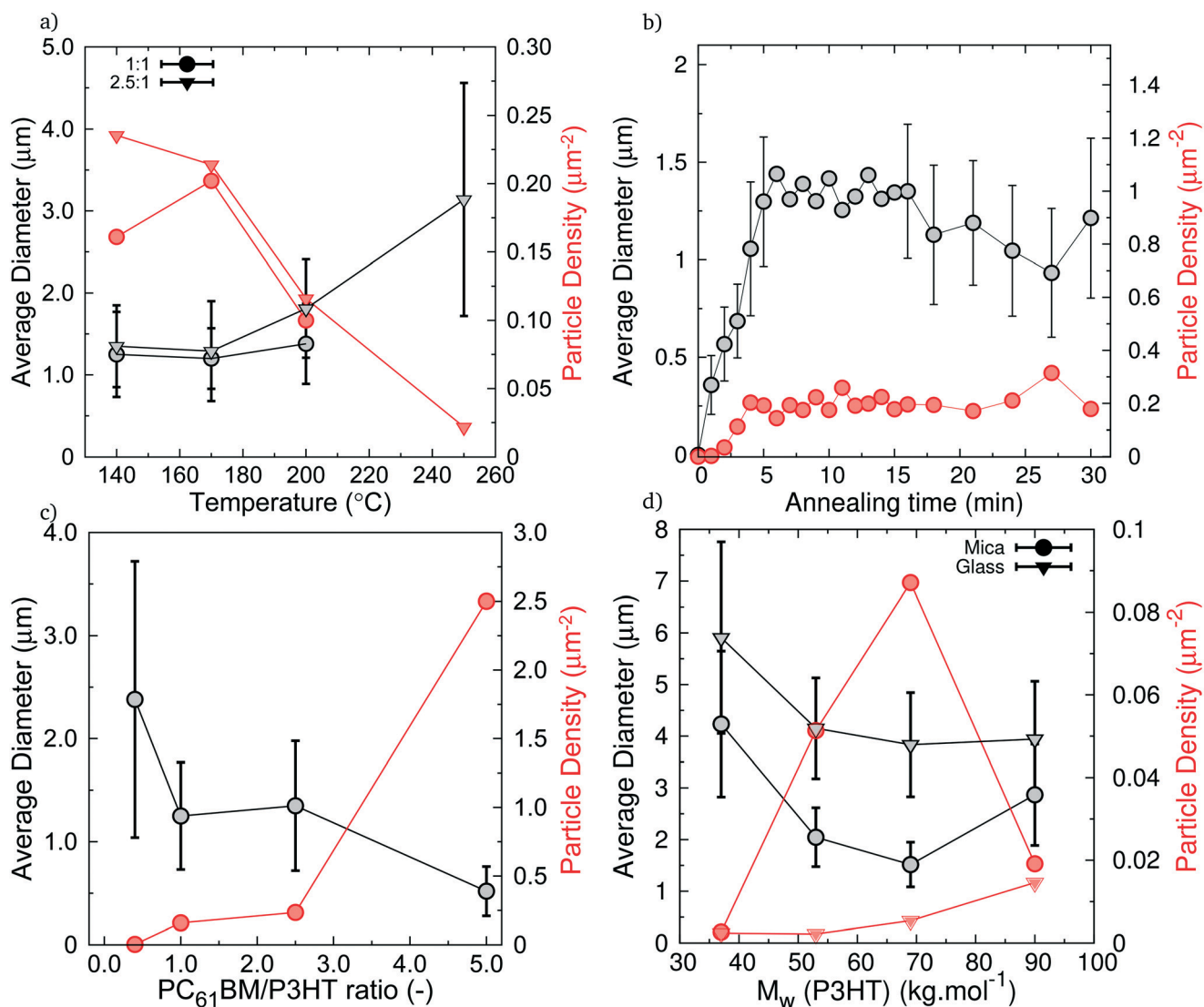

Fig. 4 Average particle diameter and particle density of $PC_{61}BM$ crystallites: (a) as a function of annealing temperature for samples produced on mica (R = 2.5 and 1). (b) As a function of annealing time for samples produced on mica (T = 140 °C). Error bars indicate standard deviation. Between 5 and 15 min the error bars are identical to that at 5 min and are left out to increase visibility. (c) As a function of the $PC_{61}BM$ over P3HT ratio (R) in the blend for samples produced on mica (T = 140 °C). (d) As a function of the P3HT molecular weight used in the blend for samples produced on glass and mica substrates (R = 1, T = 140 °C).

Fig. 4b shows the time-dependent average diameter and particle density during annealing at $T = 140$ °C for samples produced on mica. The fact that the particle density remains constant at about 0.4 particles per μm^2 after 4 minutes indicates that the particles do not cluster upon prolonged growth. Therefore, the measured particle density actually represents the nucleation density of the $PC_{61}BM$ crystallites on the mica growth template. Additionally, Fig. 4b clarifies that the crystallites do not cluster, because their growth abruptly stops at an average diameter of about 1.5 μm shortly after the nucleation density reaches its highest level. The abrupt halt of crystal growth might be explained by the fact that the area around the crystal nuclei becomes depleted from PC_{61}-BM allowing easy clustering of P3HT which in turn further hampers the diffusion of $PC_{61}BM$ towards the crystallites. The effect of P3HT crystallisation on the nucleation of PC_{61}-BM is elaborated in more detail later in this paper and in the ESI.†

3.3 Blend composition

Samples produced from blends with $R < 0.4$ showed no PC_{61}-BM crystallites, regardless of the substrate type or annealing temperature. For samples produced on glass from a blend with $R > 1$, large $PC_{61}BM$ whiskers with lengths of hundreds of micrometres were observed for all annealing temperatures above 110 °C. On mica, however, small round-like structures were formed from the $R = 2.5$ blend, while for $R = 5$ whiskers were only formed when the annealing temperature exceeded 200 °C. Below this temperature, very densely packed round-like structures were formed. Because of the dense packing, these structures were nearly unobservable with PCM, but could be easily visualized using AFM (see the ESI†).

Fig. 4c shows the average particle diameter and particle density of $PC_{61}BM$ crystallites, as a function of the $PC_{61}BM$ over P3HT ratio (R), for samples produced on mica. In general, the particle density increases with increasing R since nucleation is dependent on the $PC_{61}BM$ supersaturation. However, going from $R = 1$ to $R = 2.5$, the differences in particle density and average crystal diameter are small and insignificant compared to the random variations and inhomogeneities over the sample surface (indicated with error bars in Fig. 4b). The higher $PC_{61}BM$ content of the $R = 2.5$ blend apparently does not provide significantly more nucleation sites or smaller crystallites. Further increase of the $PC_{61}BM$ content, however, increases the particle density by an order of magnitude and decreases the average crystal diameter by approximately a factor 2.

3.4 Polymer properties

Crystallisation of $PC_{61}BM$ from a blend is, next to the blend composition and annealing temperature, also reported to be largely influenced by the properties of the polymer component (P3HT) in the blend.[27] The chain length of the polymer influences the blend viscosity and therefore the $PC_{61}BM$ diffusion rate, as well as the solvent evaporation rate. The latter,

in combination with the polymer chain length, polymer regioregularity and other polymeric properties, determines the polymer's crystallinity, which also influences $PC_{61}BM$ diffusion through the polymer matrix. Crystallisation of P3HT is known to start already prior to thermal annealing[8,42,43] and is significantly increased during annealing.[44,45] Consequently, it influences $PC_{61}BM$ crystallisation which, as shown in Fig. 4b, for the conditions applied in the present study, crystallizes within the first six minutes of annealing. We examined the influence of P3HT crystallisation on the nucleation and crystallisation of $PC_{61}BM$ by systematically varying the RR of P3HT, while keeping other polymer properties constant (see the ESI†). However, this experiment did not yield conclusive results regarding the influence of the RR of P3HT on the nucleation and crystallisation of $PC_{61}BM$.

The results of an experiment investigating the influence of P3HT molecular weight on the nucleation and crystallisation of $PC_{61}BM$ on glass and mica are presented in Fig. 4d. On a glass substrate, nucleation increased slightly with increasing molecular weight, and the average crystallite diameter stayed roughly constant. On mica, for the highest and lowest molecular weights, the influence of the nucleation enhancing effect of the mica template seems limited, since the average diameter and particle density were similar to those on glass. However, the enhancement becomes more pronounced at an intermediate P3HT molecular weight, where the particle density is raised by at least a factor 10, compared to samples produced on glass. A minimum average diameter and maximum particle density is observed for samples with P3HT of $M_w^{P3HT} = 69$ kg mol^{-1}. Overall, when increasing the molecular weight, for samples on mica, the $PC_{61}BM$–P3HT interaction parameter increases, leading to decreased miscibility between the two components. This promotes the aggregation of $PC_{61}BM$[46] up to a $M_w^{P3HT} = 69$ kg mol^{-1} threshold. Beyond this threshold, however, the increased blend viscosity apparently hampers $PC_{61}BM$ diffusion and subsequently nucleation.

3.5 Transfer

Active layers produced from a standard blend ($R = 1$, $T = 140$ °C) on mica were transferred to ZnO-coated ITO patterned glass substrates using water transfer. It was found that the strong interaction of water with a cleaved mica surface results in an easy float-off of the active layer when the coated mica substrate is submerged in nano-pure water. Active layers down to 50 nm thick floated on the water and could subsequently be picked up with the ZnO-coated ITO/glass substrate (a video showing this process is included in the ESI†). Initial manual manipulation of the substrate during transfer frequently resulted in ripping and folding of the active layer. This could be prevented by small improvements in the set-up. In the improved set-up shown in Fig. 5a, the position of both substrates are fixed by clamps while the water bath with lateral dimensions slightly larger than those of the substrates was gradually moved upwards with a precision controlled
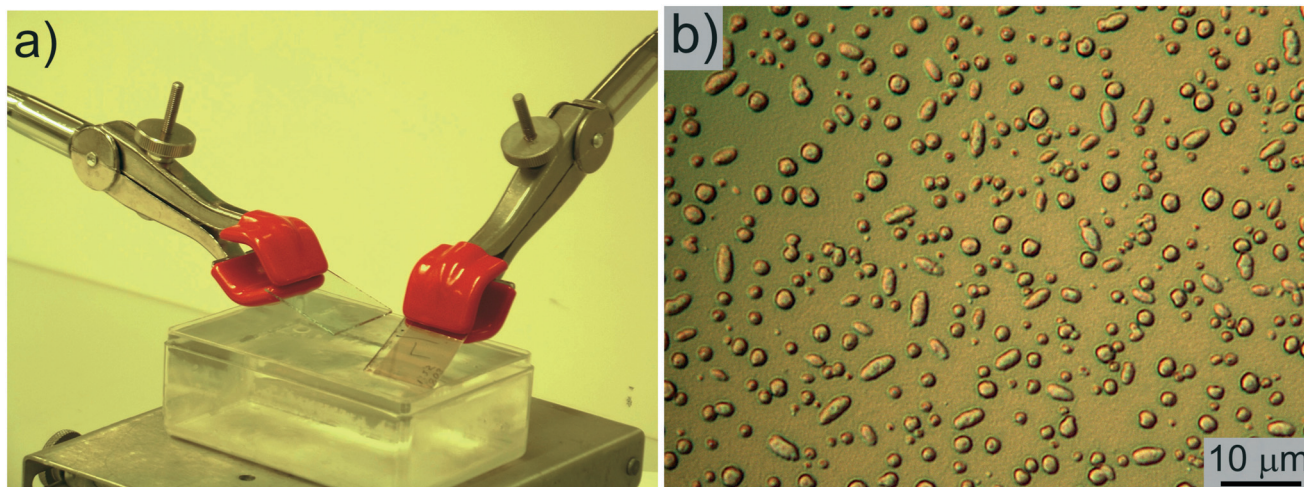
Fig. 5 Active layer transfer from a mica growth template to a ZnO-coated ITO-glass substrate showing a) the transfer set-up with two clamps for holding both substrates and a nano-pure water bath which can be moved upwards in a precisely controlled way and b) an optical microscopy image of a transferred active layer.

lab-jack (Fig. 5a). After transfer, residual water was removed by drying at 90 °C on a hotplate in air. Fig. 5b shows an optical PCM image of a transferred active layer, indicating a similar structure to that typically observed before transfer.

3.6 Device performance

As a proof of concept, an active layer spin-coated (and annealed) on mica was transferred to a ZnO-coated ITO substrate and fabricated into an inverted solar cell. Fig. 6 shows IV characteristics, external quantum efficiency (EQE) curves and the device architecture of the transferred inverted solar cell and a conventional inverted solar cell. The latter was produced directly on the ZnO coating, with identical preparation parameters and annealing conditions to the first, and reached an efficiency of 1.8%. The transferred cell outperforms the conventional cell mainly because of a 22% higher short-circuit current (as is also shown by the EQE measurements) leading to a PCE of 2.1%. The open-circuit voltages are nearly identical for both cells, which both show fill factors of above 55%, indicating that indeed, soundly operating solar cells were prepared. The lower FF of the transferred cell is associated with a lower parallel resistance of the cell, as can be deduced from the inclination of the IV curves with the
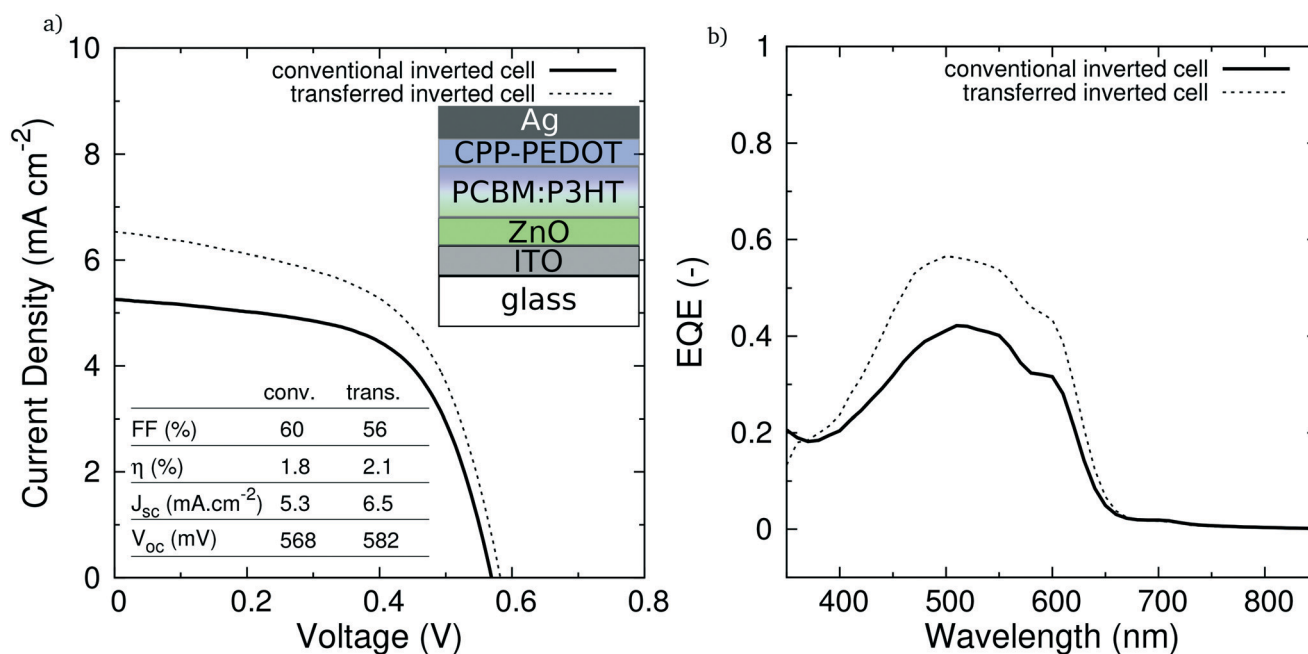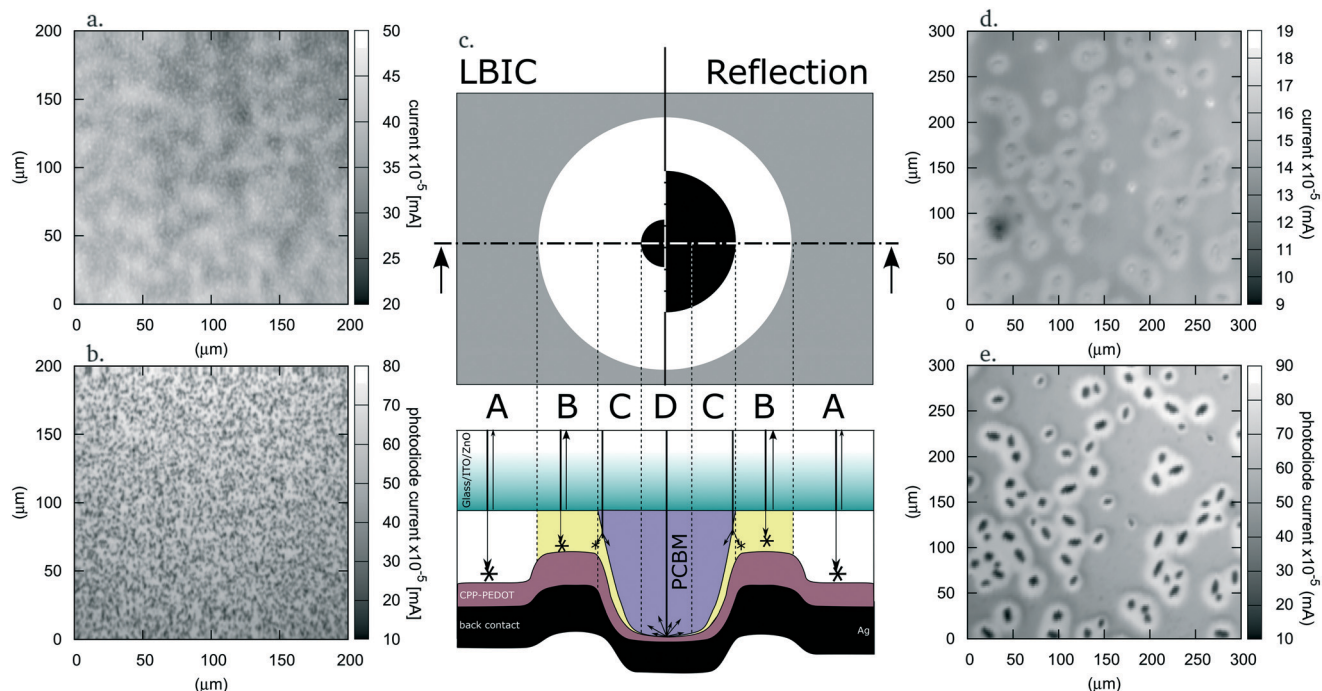

Fig. 6 Current–voltage characteristics (a) and external quantum efficiency (b) of a transferred (CHJ) inverted solar cell and a conventional (BHJ) inverted solar cell, both with the shown layer structure. Active layer production parameters for both cells: $R = 1$, $T = 140$ °C.

Fig. 7 LBIC (a and d) and reflection (b and e) maps of a 200 × 200 μm^2 area (a and b) of the transferred (CHJ) inverted organic solar cell with a structure shown in Fig. 6a and a 300 × 300 μm^2 area (d and e) of a transferred (CHJ) inverted organic solar cell specifically fabricated for LBIC purposes (fabrication parameters are $R = 1$, $T = 140$ °C, $M_w^{P3HT} = 31$ kg mol^{-1} and blend concentration 40 mg ml^{-1}). Furthermore, a schematic representation (c) of a PC$_{61}$BM crystallite in the active layer of a CHJ cell structure in cross-section (bottom part) along the stripe-dot line and the resulting LBIC (top, left-hand side) as observed from above are shown. The arrows in the cross-section represent the incident light that is partly reflected resulting in the reflection image on the upper right-hand side and partly absorbed in the active layer (indicated by the asterisks), eventually invoking a local current density distribution shown as visualized by the LBIC image on the upper left-hand side. Relative to the position of the PC$_{61}$BM particle, different zones are identified: general medium (A), depletion zone (B), crystallite edge (C) and crystallite centre (D).

current density axis in Fig. 6. This might be due to small pinholes formed during the transfer procedure.

Laser beam induced current (LBIC) was used to identify the spatial distribution of the generated current in the produced solar cells. Fig. 7a shows the current map of a 200 × 200 μm^2 part of the transferred inverted solar cell for which the IV and QE characteristics are shown in Fig. 6. The LBIC image can be compared to the reflection image of the device (Fig. 7b). The latter was simultaneously measured with the current map and indicates the direct reflection from the surface (which is observed as a current measured with a photodiode). However, from Fig. 7a and b it is difficult to draw a clear conclusion about the generated current density in relation to the location of the crystallites since the LBIC resolution (of 1 μm) does not allow a sufficiently detailed observation of features in our crystallite size range. Therefore, a transferred inverted solar cell dedicated for LBIC measurement was fabricated using a higher concentration blend (40 mg ml^{-1} instead of 20 mg ml^{-1}) and P3HT ($M_w = 31$ kg mol^{-1}, Rieke Materials), which allows for low density growth of large crystallites. As anticipated, the active layer of this cell showed significantly larger PC$_{61}$BM crystallites yielding an easily distinguishable signature in the LBIC map (see Fig. 7d).

As expected, generation of a locally reduced current is observed at the location of the crystallites because PC$_{61}$BM does

not absorb light. On the other hand, a distinct circular area (current ring) of enhanced current density is observed around the PC$_{61}$BM crystallites. The enhanced current generation takes place despite the fact that the same areas also reflect more light as is clear from the simultaneously recorded reflection image in Fig. 7e. Based on the 10–20 nm exciton diffusion length in bulk heterojunction solar cells,[47] an enhanced current density might be anticipated in an area around the PC$_{61}$BM crystallites. However, for the transferred controlled morphology cell shown in Fig. 7 this area of enhanced current density has a width as large as 10 μm around the crystallites, indicating other processes are contributing to the observed result. It is important to note here that our LBIC resolution is 1 μm and the observed rings exceed this resolution, meaning they are not artefacts resulting from our measurement set-up. Also, Fig. 7 shows that, in general, smaller PC$_{61}$BM crystallites have more enhancement in current density (intenser rings) compared to the larger crystallites.

4 Discussion

Li *et al.*[26] attributed the preferred nucleation and crystallisation of PC$_{61}$BM on the cleaved surface of (001) muscovite mica to the existence of an epitaxial relation. The cleaved (001) surface of mica consists of hexagonally oriented

oxygen atoms, which are spaced 4.6 Å apart, meaning that the smallest hexagon that can be distinguished has a diameter of 9.2 Å (see the ESI†). Since a Buckminsterfullerene molecule has similar dimensions, the $PC_{61}BM$ molecule might indeed form a growth nucleus with a preferred orientation with respect to the hexagon of oxygen atoms at the mica surface. So far however, the exact lattice structure of $PC_{61}BM$ on mica has not been resolved.[48–51] Based on the nucleus to nucleus diameter of 7.1 Å for a C_{60} in $PC_{61}BM$, Li et al.[26] and Zheng et al.[27] proposed that $PC_{61}BM$ on (001) mica nucleates in a distorted cubic structure.[36] For systems with a high $PC_{61}BM$ concentration, twinning of this cubic structure was suggested to result in pentagon-shaped crystallites. However, it is common practise to use the Van Der Waals diameter to describe the crystallisation of organic molecules on substrates.[52,53] Based on the 10.2 Å Van Der Waals diameter of a C_{60} in PC_{61}-BM, we found that a hexagonal structure would be a more probable configuration for the epitaxial relation between PCBM and mica. This structure agrees well with the observations of macro-scale hexagon-shaped $PC_{61}BM$ crystallites (see Fig. 3). Although in particular at lower temperatures the PC_{61}-BM grains still reveal a more rounded shape, TEM analysis of layers produced under the same conditions used to produce the solar cells ($R = 1$, $T = 140$ °C) reveals an electron diffraction pattern that also indicates a hexagonal rather than a cubic packing structure. This also indicates that there is an epitaxial relation between the $PC_{61}BM$ and (001) mica explaining the increased nucleation as compared to other substrates. We aimed for further confirmation of the $PC_{61}BM$/mica template relation by XRD analysis but this was unsuccessful because of the limited $PC_{61}BM$ crystal volume of the samples. However, with PCM the preferred threefold symmetric alignment of crystallites on the mica substrate can be clearly identified (see the ESI†). The hexagonal structure of $PC_{61}BM$ and the epitaxial relation to the mica template is further elaborated in the ESI.†

4.1 LBIC results

For the LBIC analysis, it is important to note that in this study we simultaneously measure the cell current and observe the reflection from the bottom side of the $PC_{61}BM$ crystallites. The schematic model of the area around a $PC_{61}BM$ crystallite as shown in Fig. 7c will be used to interpret our observations as shown in Fig. 7. In the images of Fig. 7d and e (in particular the reflection image), areas with three clearly different intensities can be distinguished. For convenience, we will refer to these areas as white, grey and black, and as such they are also represented in the schematic LBIC and reflection images at the top part of Fig. 7c. Based on the relative distance with respect to the $PC_{61}BM$ crystallite, a location in the active layer is referred to as general medium, depletion zone, crystallite edge and crystallite centre. In Fig. 7c, these areas are indicated by A, B, C and D, respectively.

In LBIC, an intermediate signal level (grey) is obtained from the general medium. This part simply functions like a

mixed bulk heterojunction cell. The depletion zone (white) yields a higher current density than the general medium. Related to the formation of the crystallite, this zone is expected to be depleted from $PC_{61}BM$, as also suggested by the growth mechanism deduced from Fig. 4b, as described at the end of section 3.2. This depletion results in a locally thinner layer[54–57] with supposedly an enhanced crystalline nature of P3HT (indicated by the yellow area in Fig. 7). Apparently this results in higher current generation than that obtained in the general medium.

Finally, the crystal center (black) contributes least to the LBIC signal since $PC_{61}BM$ absorbs little light, resulting in a minimal current generation in this area. It should be noted that a fraction of the light entering at the bottom side of a $PC_{61}BM$ crystallite ultimately can be scattered towards another part of the active layer structure (see Fig. 7). There, it can still be absorbed and contribute to the current generation of the cell which explains that the LBIC signal at the centre of a $PC_{61}BM$ crystallite is low but not zero. In terms of reflection, the general medium area (gray) shows intermediate reflection. Related to the low $PC_{61}BM$ content, the depletion zone is expected to have an enhanced P3HT crystallinity which would explain the enhanced reflection (white). Both the crystal edge and center areas hardly show any reflection (black) since the surface of the PCBM crystallite (the part connected to the Ag back electrode) exhibits very low specular reflection in the direction normal to the substrate.

4.2 Power conversion efficiency

The 1.8% solar cell efficiency for the inverted conventional cell reported in the present study is significantly lower than the current standard for this particular combination of materials which, for a regular cell configuration, holds an efficiency record of 6.8%.[58] The fact that our inverted conventional cell underperforms compared to this record is related to our non-optimal processing facility (see device processing) and the fact that we have used commercially available P3HT rather than purified, dedicated for OPV cell production, material. Taking this into account, the 2.1% transferred inverted cell reported in the current study actually is rather good compared to the best transferred regular cell with an efficiency of 2.23% reported by Li et al.,[26] in particular since the process steps we applied for the production of the transferred cell have not been elaborated yet.

Further optimization of the transfer process (e.g. substrate pre-treatment, annealing temperature and duration) and, more importantly, optimization of the controlled active layer morphology (e.g. by solvent engineering and tuning the annealing time to produce a layer with small homogeneously sized and distributed crystallites) may result in further improvements in cell performance. If the crystallite dimensions can be brought down to the desired length scale for exciton diffusion (i.e. near 20 nm) and a photo-active acceptor (like $PC_{71}BM$ or similar) is

used, the PCEs of present-day $PC_{61}BM:P3HT$ cells might be matched or even surpassed.

5 Conclusion

In this study, we used a dedicated growth template to study the controlled formation of the active layer structure of OPV cells. For this purpose, (001) muscovite mica was applied to produce fullerene:thiophene–polymer active layer structures by spin-coating of a $PC_{61}BM:P3HT$ solution and subsequent annealing. The morphology of the thus-obtained $PC_{61}BM$ crystallites was found to depend strongly on the $PC_{61}BM$:P3HT ratio of the blend and the annealing temperature. The parameter range for which layers with high surface density of (sub)micrometer sized crystallites could be produced was demonstrated to be significantly larger for mica than for other substrates.

The preferred nucleation on mica is attributed to the existence of an epitaxial relation between the mica surface and $PC_{61}BM$. Related to the 10.2 Å van der Waals diameter, it was shown that $PC_{61}BM$ is expected to crystallize in a hexagonal structure on the (001) mica template rather than in a distorted cubic structure, as was previously reported in the literature. The occurrence of the hexagonal lattice was confirmed by the microscopic identification of hexagonally shaped $PC_{61}BM$ crystallites and TEM diffraction analysis.

We successfully developed a float-off procedure in water to transfer the active layers from the non-conductive mica growth template to a ZnO coated ITO-glass substrate. Subsequent device processing resulted in a transferred inverted solar cell with a power conversion efficiency of 2.1%. Mainly because of a 22% higher short-circuit current density, the transferred cell outperforms its conventional counterpart (efficiency 1.8%) for which the active layer structure was directly produced on the ZnO coated ITO-glass substrate.

An experimental set-up that allows for simultaneous laser beam induced current (LBIC) and surface reflection analysis was developed and applied to investigate the spatial performance of the inverted cell. This revealed that the increased current densities originate from circular areas around the $PC_{61}BM$ crystallites. The observed LBIC signature and reflection image could be explained by a model based on the assumption that the active layer directly around the $PC_{61}BM$ crystallites is depleted from $PC_{61}BM$. This yields a locally thinner layer in which the P3HT is allowed to become more crystalline in nature as well. In turn, this increasingly hampers further diffusion of $PC_{61}BM$ towards the growing $PC_{61}BM$ crystallite. The occurrence of this mechanism also explains the abrupt halt in crystal growth, as observed in the time evaluation of $PC_{61}BM$ particle formation upon annealing.

The decoupling of growth, subsequent device production and operation has shown to be a viable route to produce (organic) solar cells with an enhanced efficiency. The fact that even in this early stage of research a power conversion efficiency improvement could be obtained opens ample opportu-

nities for further investigations in this direction, but more importantly it demonstrates that the transferred PV concept is not only useful for III–V solar cells but is of a more generic nature.

Acknowledgements

References

1 M. Scharber and S. Sariciftci, *Prog. Polym. Sci.*, 2013, **38**, 1929–1940.
2 G. Dennler, M. Scharber and C. Brabec, *Adv. Mater.*, 2009, **21**, 1323–1338.
3 M. Brady, G. Su and M. Chabinyc, *Soft Matter*, 2011, **7**, 11065–11077.
4 H. Hoppe and N. Sariciftci, *J. Mater. Chem.*, 2006, **16**, 45–61.
5 X. Yang and J. Loos, *Macromolecules*, 2007, **40**, 1353–1362.
6 X. Yang, J. Loos, S. C. Veenstra, W. J. H. Verhees, M. M. Wienk, J. M. Kroon, M. A. J. Michels and R. A. J. Janssen, *Nano Lett.*, 2005, **5**, 579–583.
7 C. Ma, W. Yang, X. Gong, K. Lee and A. Heeger, *Adv. Funct. Mater.*, 2005, **15**, 1617–1622.
8 W. Ma, J. Kim, K. Lee and A. Heeger, *Macromol. Rapid Commun.*, 2007, **28**, 1776–1780.
9 S. Menke and R. Holmes, *Energy Environ. Sci.*, 2014, **7**, 499–512.
10 J. Bijleveld, V. Gevaerts, M. Di Nuzzo, D. Turbiez, S. Mathijssen, D. de Leeuw, M. Wienk and R. Janssen, *Adv. Mater.*, 2010, **22**, E242–E246.
11 H. W. Ro, B. Akgun, B. T. O'Connor, M. Hammond, R. J. Kline, C. R. Snyder, S. K. Satija, A. L. Ayzner, M. F. Toney, C. L. Soles and D. M. DeLongchamp, *Macromolecules*, 2012, **45**, 6587–6599.
12 M. Campoy-Quiles, T. Ferenczi, T. Agostinelli, P. Etchegoin, Y. Kim, T. Anthopoulos, P. Stavrinou, D. Bradley and J. Nelson, *Nat. Mater.*, 2008, **7**, 158–164.
13 P. Kohn, Z. Rong, K. Scherer, A. Sepe, M. Sommer, P. Müller-Buschbaum, R. Friend, U. Steiner and S. Hüttner, *Macromolecules*, 2013, **46**, 4002–4013.
14 N. Treat, M. Brady, G. Smith, M. Toney, E. Kramer, C. Hawker and M. Chabinyc, *Adv. Energy Mater.*, 2011, **1**, 82–89.
15 D. Spoltore, W. Oosterbaan, S. Khelifi, J. Clifford, A. Viterisi, E. Palomares, M. Burgelman, L. Lutsen, D. Vanderzande and J. Manca, *Adv. Energy Mater.*, 2013, **3**, 466–471.
16 N. Seidler, G. Lazzerini, G. Destri, G. Marletta and F. Cacialli, *J. Mater. Chem. C*, 2013, **1**, 7748–7757.

17 C. Poelking and D. Andrienko, *Macromolecules*, 2013, **46**, 8941–8956.

18 F. Yang, M. Shtein and S. Forrest, *Nat. Mater.*, 2005, **4**, 37–41.

19 U. W. Paetzold, W. Qiu, F. Finger, J. Poortmans and D. Cheyns, *Appl. Phys. Lett.*, 2015, **106**, 173101.

20 J. Xu, Z. Hu, K. Zhang, L. Huang, J. Zhang and Y. Zhu, *Energy Technol.*, 2015, **315211**, 314–318.

21 G. Fan, X. Yang, R. Liang, J. Zhao, S. Li and D. Yan, *CrystEngComm*, 2016, **18**, 240–249.

22 D. Yan, A. Delori, G. O. Lloyd, B. Patel, T. Friscic, G. M. Day, D.-K. Bucar, W. Jones, J. Lu, M. Wei, D. G. Evans and X. Duan, *CrystEngComm*, 2012, **14**, 5121–5123.

23 D. Yan, *Chem. – Eur. J.*, 2015, **21**, 4880–4896.

24 D. Yan and D. G. Evans, *Mater. Horiz.*, 2014, **1**, 46–57.

25 D. Yan, W. Jones, G. Fan, M. Wei and D. G. Evans, *J. Mater. Chem. C*, 2013, **1**, 4138–4145.

26 L. Li, G. Lu, S. Li, H. Tang and X. Yang, *J. Phys. Chem. B*, 2008, **112**, 15651–15658.

27 L. Zheng, J. Liu and Y. Han, *Phys. Chem. Chem. Phys.*, 2013, **15**, 1208–1215.

28 J. Schermer, P. Mulder, G. Bauhuis, M. Voncken, J. Van Deelen, E. Haverkamp and P. Larsen, *Phys. Status Solidi A*, 2005, **202**, 501–508.

29 G. Bauhuis, P. Mulder, E. Haverkamp, J. Huijben and J. Schermer, *Sol. Energy Mater. Sol. Cells*, 2009, **93**, 1488–1491.

30 M. Green, K. Emery, Y. Hishikawa, W. Warta and E. Dunlop, *Progr. Photovolt.: Res. Appl.*, 2015, **23**, 1–9.

31 F. C. Krebs, N. Espinosa, M. Hösel, R. R. Søndergaard and M. Jørgensen, *Adv. Mater.*, 2014, **26**, 29–39.

32 S. K. Hau, H. Yip, N. Baek, J. Zou, K. O'Malley and A.-Y. Jen, *Appl. Phys. Lett.*, 2008, **92**, 253301.

33 C. Lindqvist, A. Sanz-Velasco, E. Wang, O. Bäcke, S. Gustafsson, E. Olsson, M. Andersson and C. Müller, *J. Mater. Chem. A*, 2013, **1**, 7174–7180.

34 Y. Sun, J. H. Seo, C. J. Takacs, J. Seifter and A. J. Heeger, *Adv. Mater.*, 2011, **23**, 1679–1683.

35 D. Pashley, *Adv. Phys.*, 1956, **5**, 173–240.

36 Y. Kim, J. Nelson, T. Zhang, S. Cook, J. Durrant, H. Kim, J. Park, M. Shin, S. Nam and M. Heeney, *ACS Nano*, 2009, **3**, 2557–2562.

37 J. Zhao, A. Swinnen, G. V. Assche, J. Manca, D. Vanderzande and B. V. Mele, *J. Phys. Chem. B*, 2009, **113**, 1587–1591.

38 T. Ngo, D. Nguyen and V. Nguyen, *Adv. Nat. Sci.: Nanosci. Nanotechnol.*, 2012, **3**, 045001.

39 J. Zhao, A. Swinnen, G. Van Assche, J. Manca, D. Vanderzande and B. V. Mele, *J. Phys. Chem. B*, 2009, **113**, 1587–1591.

40 K. Lee, Y. Zhang, P. Burn, I. Gentle, M. James, A. Nelson and P. Meredith, *J. Mater. Chem. C*, 2013, **1**, 2593–2598.

41 X. Yang, A. Alexeev, M. Michels and J. Loos, *Macromolecules*, 2005, **38**, 4289–4295.

42 D. Motaung, G. Malgas, C. Arendse, S. Mavundla, C. Oliphant and D. Knoesen, *J. Mater. Sci.*, 2009, **44**, 3192–3197.

43 E. Verploegen, R. Mondal, C. Bettinger, S. Sok, M. Toney and Z. Bao, *Adv. Funct. Mater.*, 2010, **20**, 3519–3529.

44 S. Lilliu, T. Agostinelli, E. Pires, M. Hampton, J. Nelson and J. Macdonald, *Macromolecules*, 2011, **44**, 2725–2734.

45 T. Agostinelli, S. Lilliu, J. Labram, M. Campoy-Quiles, M. Hampton, E. Pires, J. Rawle, O. Bikondoa, D. Bradley and T. Anthopoulos, *Adv. Funct. Mater.*, 2011, **21**, 1701–1708.

46 F. Liu, D. Chen, C. Wang, K. Luo, W. Gu, A. Briseno, J. Hsu and T. Russell, *ACS Appl. Mater. Interfaces*, 2014, **6**, 19876–19887.

47 P. E. Shaw, A. Ruseckas and I. D. Samuel, *Adv. Mater.*, 2008, **20**, 3516–3520.

48 X. Yang, J. van Duren, M. Rispens, J. Hummelen, R. Janssen, M. Michels and J. Loos, *Adv. Mater.*, 2004, **16**, 802–806.

49 E. Schwartz, T. Muir, A. Tyszkiewicz, P. Power, M. Abu-Omar, A. Fürstner, V. Mamane, P. Barrett, T. Boix and M. Puche, *Chem. Commun.*, 2003, 2090.

50 D. Écija, R. Otero, L. Sánchez, J. Gallego, Y. Wang, M. Alcam, F. Martn, N. Martn and R. Miranda, *Angew. Chem.*, 2007, **119**, 8020–8023.

51 Y. Wang, M. Alcam and F. Martn, *ChemPhysChem*, 2008, **9**, 1030–1035.

52 S. Forrest, *Chem. Rev.*, 1997, **97**, 1793–1896.

53 D. Hooks, T. Fritz and M. Ward, *Adv. Mater.*, 2001, **13**, 227–241.

54 K. Maturová, R. A. Janssen and M. Kemerink, *ACS Nano*, 2010, **4**, 1385–1392.

55 H. Zhong, X. Yang, B. Dewith and J. Loos, *Macromolecules*, 2006, **39**, 218–223.

56 X. Yang, J. K. van Duren, R. A. Janssen, M. A. Michels and J. Loos, *Macromolecules*, 2004, **37**, 2151–2158.

57 C. Bulle-Lieuwma, J. van Duren, X. Yang, J. Loos, A. Sieval, J. Hummelen and R. Janssen, *Appl. Surf. Sci.*, 2004, **231**, 274–277.

58 S. Lee, J. Kim, T. Shim and J. Park, *Electron. Mater. Lett.*, 2009, **5**, 47–50.